Author for correspondence:
D. Holdenried-Chernoff
e-mail:
daria.holdenried@erdw.ethz.ch

A trio of simple optimised axisymmetric kinematic dynamos in a sphere

D. Holdenried-Chernoff [1], L. Chen[2] and A. Jackson[1]

[1]Institut für Geophysik, ETH Zurich, Sonneggstrasse 5, 8092 Zürich, Switzerland

[2] Department of Mathematical Sciences, Durham University, DH1 3LE, UK

Planetary magnetic fields are generated by the motion of conductive fluid in the planet's interior. Complex flows are not required for dynamo action; simple flows have been shown to act as efficient kinematic dynamos, whose physical characteristics are more straightforward to study. Recently, Chen et al. (2018, J. Fluid Mech., 839, 1-32) found the optimal, unconstrained kinematic dynamo in a sphere, which, despite being of theoretical importance, is of limited practical use. We extend their work by restricting the optimisation to three simple two-mode axisymmetric flows based on the kinematic dynamos of Dudley and James (1989, Proc. R. Soc. A., 425, 407-429). Using a Lagrangian optimisation, we find the smallest critical magnetic Reynolds number for each flow-type, measured using an enstrophy-based norm. A Galerkin method is used, in which the spectral coefficients of the fluid flow and magnetic field are updated in order to maximise the final magnetic energy. We consider the $t_1^0 s_1^0$, $t_1^0 s_2^0$ and $t_2^0 s_2^0$ flows and find enstrophy-based critical magnetic Reynolds numbers of 107.7, 142.4 and 125.5 (13.7, 19.6 and 16.4 respectively with the energy-based definition). These are up to four times smaller than the original flows. These simple and efficient flows may be used as benchmarks in future studies.

1. Introduction

The Earth's magnetic field and the processes responsible for the generation of planetary dynamos have been investigated for hundreds of years [1], with Joseph Larmor first proposing the currently accepted dynamo theory exactly one century ago [2]. While dynamo action is fully described using the equations of magnetohydrodynamics (MHD), solving these equations in the parameter regime relevant to Earth requires resolution on vastly different spatial and temporal scales to those that are currently computationally possible.

Given that it is not possible to study the MHD equations in the parameter regime relevant to an Earth-like setting through direct numerical simulation (DNS) [1], it can be insightful to consider a simplified system. In this vein, we adopt the kinematic dynamo approximation, where we study the very basic interactions between the motion of conductive fluid and the resulting magnetic field. A steady velocity is prescribed, and the resulting magnetic field studied. The back-reaction of the magnetic field on the flow is negligible at the onset.

One of the earliest attempts at generating a kinematic dynamo was undertaken by Bullard and Gellman [4]. They selected a simple velocity field composed of two modes, one poloidal and one toroidal, motivated by computational restrictions and by dynamics. Despite promising preliminary results, their solutions were found not to converge when computed at higher resolution. The first convergent growing numerical solutions to the induction equation in a sphere were found by G.O. Roberts [5] and Gubbins [6]. Since then, many numerical kinematic dynamo studies have been successfully conducted (e.g. Pekeris et al. [7], Kumar and Roberts [8]). Of particular note are the two-mode flows of Dudley and James [9], subsequently referred to as DJ flows, which are some of the simplest and most efficient velocity fields demonstrated to produce kinematic dynamo action.

Some of these studies took careful consideration of the physical motivation for the different flow patterns which might be capable of sustaining a dynamo. However, to find the most efficient flows, a more systematic approach must be undertaken. Efficiency is measured according to the magnetic Reynolds number, Rm, a dimensionless parameter which is a measure of the relative strength of inductive, field-creating processes compared to ohmic dissipation in the system. More efficient flows require a smaller Rm to produce dynamo action. In keeping with the work of Chen et al. [10], we use an enstrophy-based Rm, defined in section 2(a). Variational optimisation using a direct adjoint looping is well suited to seeking these efficient flows, and has been widely used in studies of flows' transition to turbulence ([11], [12]), as well as in oceanography, thermoacoustics and weather forecasting [13].

In this paper, we define an objective functional quantifying the efficiency of the dynamo, which is extremised by iteratively updating the velocity and initial magnetic field subject to various constraints. Willis [14] was the first to implement this variational optimisation technique to flows in a periodic box, achieving one of the lowest minimal Rm dynamo thresholds, Rm_c, ever observed. This was extended by Chen et al. [15] to a finite cubic domain, while Chen et al. [10] found the most efficient kinematic dynamo in a sphere. Both these optimisations produced flows with much lower Rm_c than previously considered kinematic dynamos. One of the natural extensions to this work is the optimisation of the purely axisymmetric DJ flows. Making use of the code developed by Chen et al. [10], we show that the three DJ-type flows can be optimised to be more efficient, displaying growing solutions for significantly reduced values of enstrophy-based Rm. The significance of this result lies in its improvement of the theoretical limits for dynamo action in a restricted symmetry class, as well as providing simple benchmark flows which may be used in further computation or even for future experimental kinematic dynamo studies. These simple flows can be generated more easily than complicated flows with a large number of modes, so they could be used in an attempt to produce an efficient laboratory dynamo, similar in design to the von Kármán Sodium (VKS) experiment of Monchaux et al. [16].

2. Variational optimisation of flows in a sphere

The work presented in this paper exploits the techniques and code developed by Chen et al. [10], with some modification to only consider the subspace of interest. A brief overview of the method is given below.

(a) Background

The simplest system that can be used to model a planetary dynamo is a spherical region V with boundary Σ filled with electrically conducting fluid. The region exterior to the sphere, $\hat{V}$, is current free and extends to infinity. The aim of our study is to find the axisymmetric flows which produce the fastest growing magnetic field for a given set of parameters, and thus the most efficient axisymmetric kinematic dynamos in a sphere. The magnetic field's time evolution is described by the induction equation:

$$\frac{\partial \mathbf{B}^*}{\partial t^*} = \nabla^* \times (\mathbf{U}^* \times \mathbf{B}^*) + \eta^* \nabla^2 \mathbf{B}^* \tag{2.1}$$

where $\mathbf{U}^*(\mathbf{x}^*)$ is the fluid velocity, $\mathbf{B}^*(\mathbf{x}^*, t^*)$ is the magnetic field, $\mathbf{x}^*$ is the position vector, $\eta^* = 1/(\mu_0^* \sigma^*)$ is the magnetic diffusivity of the fluid, μ_0^* is the magnetic permeability of free space and σ^* is the fluid's electrical conductivity. The asterisk denotes a dimensional quantity. This equation can be non-dimensionalised to give:

$$\frac{\partial \mathbf{B}}{\partial t} = Rm \nabla \times (\mathbf{U} \times \mathbf{B}) + \nabla^2 \mathbf{B} \tag{2.2}$$

where all un-starred quantities are non-dimensional. The variables have been made dimensionless by using the scalings: $[\mathbf{x}] = L^*$, $[t] = (L^*)^2/\eta^*$, $[\mathbf{B}] = B^*$ and $[\mathbf{U}] = \omega^* L^*$. L^* and η^* are the dimensional spherical radius and magnetic diffusivity, B^* is an arbitrary dimensional magnetic field scale and ω^* is the root mean square dimensional enstrophy, defined as:

$$\omega^* = \sqrt{\frac{1}{V} \int_V (\nabla \times \mathbf{U}^*)^2 \mathrm{d}V} \tag{2.3}$$

The enstrophy-based magnetic Reynolds number, Rm, is defined as:

$$Rm = \frac{\omega^* L^{*2}}{\eta^*} \tag{2.4}$$

The more traditional kinetic energy-based definition of the magnetic Reynolds number, $Rm^u = U^* L^*/\eta^*$, cannot be used when performing an optimisation, as Proctor [17] showed that there is no lower limit on Rm^u. This is because reducing the size of the fluid container (the region where $u \neq 0$) allows solutions to the induction equation for $Rm \to 0$. Therefore, it is meaningless to seek the lowest critical Rm^u for a flow, which is why we adopt the enstrophy-based Rm instead. Conversion formulae to the historically more conventional kinetic energy and strain based Rm are given in Appendix A. Since the velocity field is steady and the induction equation is linear in $\mathbf{B}$, we can use the ansatz:

$$\mathbf{B}(\mathbf{x}, t) = \sum_i a_i \mathbf{b}_i(\mathbf{x}) e^{\gamma_i t} \tag{2.5}$$

for the magnetic field, where a_i is a coefficient, $\mathbf{b}_i(\mathbf{x})$ is an eigenvector and γ_i is its growth rate. After a sufficiently long time, the most rapidly growing eigenvector should dominate the solution. At the critical magnetic Reynolds number, Rm_c, the fastest growing mode has $\Re(\gamma) = 0$, implying that either a steady or oscillatory dynamo is achieved. The lower Rm_c, the more efficient the dynamo. The growth rate of the magnetic field $\mathbf{B}$ is measured at a time T, long enough for any transient behaviour to have died away, where $\mathbf{B}(\mathbf{x}, T) = \mathbf{B}_T$. The objective functional is chosen to be the logarithm of the magnetic energy E averaged over all space, as this is a direct measure

of the magnetic field's growth rate; E is given by

$$E = \frac{1}{V + \hat{V}} \int_{V + \hat{V}} \mathbf{B}_T^2 \, \mathrm{d}V \tag{2.6}$$

The optimisation computes the velocity $\mathbf{U}$ and initial magnetic field $\mathbf{B}_0 = \mathbf{B}(\mathbf{x}, 0)$ that maximise the objective functional, subject to various constraints that enforce normalisation of the velocity and the initial magnetic field in an enstrophy and energy norm respectively, as well as requiring that the equations encapsulating the physics are satisfied. The non-dimensional equations relevant to our optimization are:

$$\nabla \cdot \mathbf{B} = 0 \qquad \mathbf{x} \in V, \hat{V} \tag{2.7} \qquad\qquad \partial_t \mathbf{B} = -\nabla \times \mathbf{E} \qquad \mathbf{x} \in V, \hat{V} \tag{2.8}$$

$$\nabla \times \mathbf{B} = 0 \qquad \mathbf{x} \in \hat{V} \tag{2.9} \qquad \mathbf{E} = \nabla \times \mathbf{B} - Rm(\mathbf{U} \times \mathbf{B}) \qquad \mathbf{x} \in V \tag{2.10}$$

where $\mathbf{E}(\mathbf{x}, t)$ is the electric field (non-dimensionalised by $[\mathbf{E}] = B^* \eta^* / L^*$). Eq. (2.7) is the solenoidal condition for the magnetic field, eq. (2.8) is Faraday's law, eq. (2.9) and eq. (2.10) are Ampère's law for the insulating and conductive regions respectively. Eqs. (2.8) and (2.10) can be combined to produce eq. (2.2). We use the equations in this primitive formulation as it simplifies the treatment of the boundary terms when taking the variation of the Lagrangian [10]. The magnetic field satisfies insulating boundary conditions and decays at least as fast as r^{-3} in the insulating region. $\mathbf{B}$ and $\mathbf{E}$ satisfy the continuity conditions:

$$\mathbf{B}|_{\Sigma+} - \mathbf{B}|_{\Sigma-} = \mathbf{0}, \qquad\qquad \hat{\mathbf{r}} \times (\mathbf{E}|_{\Sigma+} - \mathbf{E}|_{\Sigma-}) = \mathbf{0} \tag{2.11}$$

on the outer, Σ_+, and inner, Σ_-, surfaces of the sphere. The velocity field $\mathbf{U}$ is taken to be time-independent, incompressible and satisfies no-slip boundary conditions:

$$\nabla \cdot \mathbf{U} = 0, \qquad\qquad \mathbf{U}|_{\Sigma-} = \mathbf{0} \tag{2.12}$$

The complete Lagrangian for our problem, chosen by Chen et al. [10], is:

$$\mathcal{L} = \ln\langle (\mathbf{B}_T)^2 \rangle - \lambda_1 \left(\frac{1}{V} \langle (\nabla \times \mathbf{U})^2 \rangle - 1 \right) - \lambda_2 (\langle (\mathbf{B}_0)^2 \rangle - 1) - \langle \Pi \nabla \cdot \mathbf{U} \rangle - \int_0^T \langle \psi^\dagger \nabla \cdot \mathbf{B} \rangle \mathrm{d}t$$

$$- \int_0^T \langle \mathbf{B}^\dagger \cdot [\partial_t \mathbf{B} + \nabla \times \mathbf{E}] \rangle \mathrm{d}t - \int_0^T \langle \mathbf{E}^\dagger \cdot [\sigma_r \mathbf{E} + Rm \mathbf{U} \times \mathbf{B} - \nabla \times \mathbf{B}] \rangle \mathrm{d}t \tag{2.13}$$

where $\langle ... \rangle$ is an integral over all space:

$$\langle ... \rangle = \int_0^\infty \int_0^{2\pi} \int_0^\pi ... \, r^2 \sin\theta \, \mathrm{d}\theta \, \mathrm{d}\phi \, \mathrm{d}r \tag{2.14}$$

and $\lambda_1, \lambda_2, \Pi(\mathbf{x}), \psi^\dagger(\mathbf{x}, t), \mathbf{B}^\dagger(\mathbf{x}, t)$ and $\mathbf{E}^\dagger(\mathbf{x}, t)$ are Lagrange multipliers. $\mathbf{B}^\dagger(\mathbf{x}, t)$ and $\mathbf{E}^\dagger(\mathbf{x}, t)$ are referred to as the adjoint magnetic and electric fields, and satisfy the same boundary conditions as the physical fields. σ_r is the relative electrical conductivity, which is unity inside the sphere and vanishes in the exterior.

(b) Optimisation procedure

The variation of the Lagrangian (2.13) with respect to each of its variables vanishes at the optimum, producing the Euler-Lagrange equations for the system. The variation with respect to all variables except $\mathbf{U}$ and $\mathbf{B}_0$ is taken to vanish automatically, producing a system of equations that can be solved iteratively by updating the velocity and initial magnetic field in the direction of the local gradient. Adjoint methods enable the efficient calculation of the required quantities [20]. Of special note is the use of the Galerkin basis to represent the vector fields, which has a number of desirable properties. Foremost, it automatically incorporates both the boundary conditions at $r = 1$ and the solenoidality constraints, so that they do not need to be imposed separately. The

basis functions are orthonormal with respect to a chosen inner product and for smooth functions the representation converges spectrally. The velocity, magnetic field and adjoint magnetic field are expanded as:

$$\begin{bmatrix} \mathbf{U} \\ \mathbf{B} \\ \mathbf{B}^\dagger \end{bmatrix} = \sum_{n=1}^{n_{max}} \sum_{\ell=1}^{\ell_{max}} \sum_{m=-\ell}^{\ell} \begin{bmatrix} t_{nm\ell}\mathbf{U}_{nm\ell}^t + s_{nm\ell}\mathbf{U}_{nm\ell}^p \\ T_{nm\ell}\mathbf{B}_{nm\ell}^t + S_{nm\ell}\mathbf{B}_{nm\ell}^p \\ T_{nm\ell}^\dagger\mathbf{B}_{nm\ell}^t + S_{nm\ell}^\dagger\mathbf{B}_{nm\ell}^p \end{bmatrix} \tag{2.15}$$

where $t_{nm\ell}, s_{nm\ell}, T_{nm\ell}, S_{nm\ell}$ and $T_{nm\ell}^\dagger, S_{nm\ell}^\dagger$ are the spectral coefficients of the toroidal and poloidal modes. Since $\mathbf{B}$ and $\mathbf{B}^\dagger$ satisfy the same boundary conditions, they can be expanded in the same basis. The vector basis fields correspond to a standard toroidal/poloidal decomposition for divergence-free fields, given by:

$$\mathbf{U}_{nm\ell}^t(r,\theta,\phi) = \nabla \times (t_n^\ell(r)Y_\ell^m(\theta,\phi)\hat{\mathbf{r}}), \qquad\qquad \mathbf{r} \in V \tag{2.16}$$

$$\mathbf{U}_{nm\ell}^p(r,\theta,\phi) = \nabla \times \nabla \times (p_n^\ell(r)Y_\ell^m(\theta,\phi)\hat{\mathbf{r}}), \qquad\qquad \mathbf{r} \in V \tag{2.17}$$

$$\mathbf{B}_{nm\ell}^t(r,\theta,\phi) = \begin{cases} \nabla \times (\mathcal{T}_n^\ell(r)Y_\ell^m(\theta,\phi)\hat{\mathbf{r}}), & \mathbf{r} \in V \\ \mathbf{0}, & \mathbf{r} \in \hat{V} \end{cases} \tag{2.18}$$

$$\mathbf{B}_{nm\ell}^p(r,\theta,\phi) = \begin{cases} \nabla \times \nabla \times (\mathcal{P}_n^\ell(r)Y_\ell^m(\theta,\phi)\hat{\mathbf{r}}), & \mathbf{r} \in V \\ -\ell\mathcal{P}_n^\ell(1)\nabla(r^{-(\ell+1)}Y_\ell^m(\theta,\phi))), & \mathbf{r} \in \hat{V} \end{cases} \tag{2.19}$$

$t_n^\ell(r)$, $p_n^\ell(r)$, $\mathcal{T}_n^\ell(r)$ and $\mathcal{P}_n^\ell(r)$ are radial basis functions for the toroidal/poloidal parts of the velocity and magnetic field, chosen to satisfy the boundary and orthogonality conditions. The form of the radial basis functions is given in Appendix B. The index n specifies the radial basis function that is being considered, while ℓ and m represent the degree and order of the spherical harmonic associated with the component. The latter two values describe the structure of the flow; the number of distinct cells present for a given mode is determined by the difference $\ell - m$, while m controls the number of longitudinal nodes. The velocity basis functions are orthonormal with respect to the an enstrophy-based inner product:

$$\frac{1}{V}\langle (\nabla \times \mathbf{U}_{nm\ell}^t) \cdot (\nabla \times \mathbf{U}_{n'm'\ell'}^t)\rangle = \delta_{mm'}\delta_{\ell\ell'}\delta_{nn'} \tag{2.20}$$

$$\frac{1}{V}\langle (\nabla \times \mathbf{U}_{nm\ell}^p) \cdot (\nabla \times \mathbf{U}_{n'm'\ell'}^p)\rangle = \delta_{mm'}\delta_{\ell\ell'}\delta_{nn'} \tag{2.21}$$

The magnetic field basis functions are orthonormal with respect to an energy-based inner product:

$$\langle \mathbf{B}_{nm\ell}^t \cdot \mathbf{B}_{n'm'\ell'}^t\rangle = \delta_{mm'}\delta_{\ell\ell'}\delta_{nn'} \tag{2.22}$$

$$\langle \mathbf{B}_{nm\ell}^p \cdot \mathbf{B}_{n'm'\ell'}^p\rangle = \delta_{mm'}\delta_{\ell\ell'}\delta_{nn'} \tag{2.23}$$

The boundary conditions satisfied by the basis fields are:

$$t_n^\ell(1) = 0, \qquad p_n^\ell(1) = \frac{\partial p_n^\ell}{\partial r}(1) = 0, \qquad \mathcal{T}_n^\ell(1) = 0, \qquad \frac{\partial \mathcal{P}_n^\ell(1)}{\partial r} + \ell\mathcal{P}_n^\ell(1) = 0 \tag{2.24}$$

After each optimization loop, the velocity and magnetic field's spectral coefficients are updated. The toroidal and poloidal parts of the $\mathbf{B}_0$ update projected onto the Galerkin basis are:

$$\delta T_{nm\ell}(0) = \frac{\alpha_2}{2\lambda_2}(T_{nm\ell}^\dagger(0) - 2\lambda_2 T_{nm\ell}(0)) \quad \delta S_{nm\ell}(0) = \frac{\alpha_2}{2\lambda_2}(S_{nm\ell}^\dagger(0) - 2\lambda_2 S_{nm\ell}(0)) \tag{2.25}$$

where the (0) refers to coefficients of $\mathbf{B}$ and $\mathbf{B}^\dagger$ at $t = 0$.

The velocity updates are:

$$\delta t_{nm\ell} = \frac{\alpha_1}{2\lambda_1}(\mathcal{J}^t_{nm\ell} - 2\lambda_1 t_{nm\ell}) \qquad\qquad \delta s_{nm\ell} = \frac{\alpha_1}{2\lambda_1}(\mathcal{J}^p_{nm\ell} - 2\lambda_1 s_{nm\ell}) \qquad (2.26)$$

where α_1 is the step size for the velocity update and $\mathcal{J}^{t,p}_{nm\ell}$ is:

$$\mathcal{J}^{t,p}_{nm\ell} = \sum_{i=0}^{N} \beta_i \Delta t \langle \mathbf{U}^{t,p}_{nm\ell} \cdot [\mathbf{B}(\mathbf{x},t_i) \times (\nabla \times \mathbf{B}^\dagger(\mathbf{x},t_i))] \rangle \qquad (2.27)$$

β_i are integration weights set to 0.5 at $i=0, N$ and 1 otherwise. An explanation of the origin of these expressions is omitted here for brevity, but is outlined in [10]. λ_1 and λ_2 are chosen such that the velocity and initial magnetic field remain normalised according to eqs. (2.20)-(2.21) and (2.22)-(2.23). As we are interested in optimising the simplest dynamos, we restrict our attention to axisymmetric velocity modes ($m=0$) with $\ell = 1$ or 2. To ensure that the flow remains constrained to these subspaces during the optimisation, the updated flow coefficients are "projected" onto the desired ℓ and m modes by extinguishing the coefficients of other modes. The initial flows and each update vector are projected in this manner, such that the final velocity remains in the correct subspace. The optimisation loop is repeated until the total residue, r_t, is smaller than 10^{-4}, where r_t is defined by:

$$r_t = \sqrt{r_U^2 + r_{B_0}^2} \qquad (2.28)$$

with

$$r_U^2 = \sum_{nm\ell} \delta t_{nm\ell}^2 + \delta s_{nm\ell}^2 \qquad\qquad r_{B_0}^2 = \sum_{nm\ell} \delta T_{nm\ell}^2 + \delta S_{nm\ell}^2 \qquad (2.29)$$

where the δs represent the change in the toroidal and poloidal parts of the velocity and magnetic field. All optimisations are performed at resolution (ℓ_{max}, n_{max}) = (40,40), to ensure spectral convergence of the solutions. A time step of at most 10^{-4} magnetic diffusion times is used and the forward simulations are run for 2 diffusion times, i.e. $T = 2$. In this case, the velocity field is written:

$$\mathbf{U}^t(r,\theta,\phi) = \sum_{\ell,m} \nabla \times (t_\ell^m(r) Y_\ell^m(\theta,\phi)\hat{\mathbf{r}}) \qquad (2.30)$$

$$\mathbf{U}^p(r,\theta,\phi) = \sum_{\ell,m} \nabla \times \nabla \times (p_\ell^m(r) Y_\ell^m(\theta,\phi)\hat{\mathbf{r}}) \qquad (2.31)$$

where t_ℓ^m and p_ℓ^m are related to t_n^ℓ and p_n^ℓ via:

$$t_\ell^m = \sum_n t_{nm\ell} \, t_n^\ell(r) \qquad (2.32)$$

$$p_\ell^m = \sum_n s_{nm\ell} \, p_n^\ell(r) \qquad (2.33)$$

We make use of this notation to represent the flows that we optimize ($t_1^0 s_1^0$, $t_1^0 s_2^0$, $t_2^0 s_2^0$), so that our results can readily be compared to those of Dudley and James [9]. The form of these three flows as well as the radial functions defined by DJ are given in Appendix C.

3. Optimisation results

The optimisation results for the three Dudley-James type flows are given in Table 1. All three flows have quite a similar Rm_c, with $t_1^0 s_1^0$ being the most efficient flow. This is consistent with our expectations, as Chen et al. [10]'s optimum for a sphere has the greatest enstrophy contribution from the $\ell = 1$ modes, more than three times larger than that of the $\ell = 2$ modes. In the $t_1^0 s_2^0$ case, the net helicity of the flow when averaged over solid angle is zero, due to the orthogonality of the different spherical harmonic components. Helicity, the inner product of the vorticity and velocity

	$t_1^0 s_1^0$	$t_1^0 s_2^0$	$t_2^0 s_2^0$
Rm_c	107.70	142.42	125.50

Table 1. Critical enstrophy-based Rm for the optimised DJ-type flows. The $t_1^0 s_1^0$ flow acts as the most efficient dynamo, followed by $t_2^0 s_2^0$ and finally $t_1^0 s_2^0$.
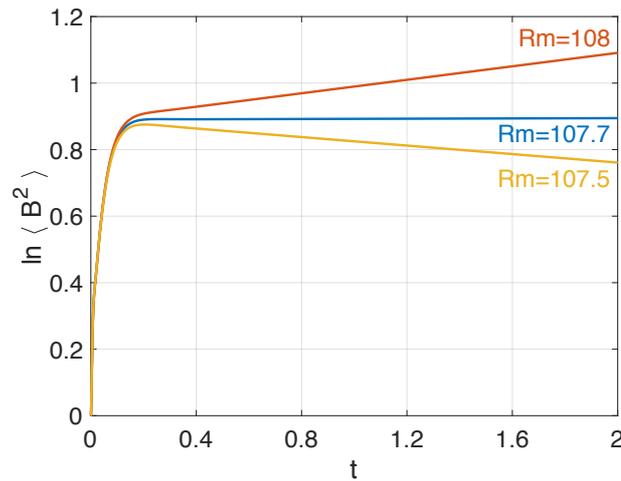
Figure 1. Plot of the logarithm of the final magnetic energy $\langle \mathbf{B}_T^2 \rangle$ of the $t_1^0 s_1^0$ flow for two magnetic diffusion times. The growth rate of the dominant eigenmode is given by the gradient in the final 100 steps of this plot, from $t = 1.99$ to 2. The red and yellow lines show a growing and decaying solution respectively. The blue line illustrates a case where the critical Rm has been found, as the growth rate is ≈ 0.

vectors, is thought to be a key ingredient for a successful kinematic dynamo [18], so it is perhaps not surprising that the $t_1^0 s_2^0$ flow is the least efficient. The results from this small sample of flows suggest that having two modes with the same spherical harmonic components, and thus a net helicity averaged over solid angle, is beneficial to creating an efficient dynamo. Furthermore, these results sustain the idea that first arose from Dudley and James' [9] work that more complicated flows are not necessarily more efficient than simpler kinematic dynamos.

(a) Verification of results

All results are checked graphically to ensure the transient behaviour has decayed within this time frame. The growth rates are measured near the end of the time interval, to avoid any transient behaviour affecting the result. Figure 1 shows an example of the plots used to extract the growth rate. Although the optima can be achieved starting from any appropriately constrained random field, seeking the optimum in this manner is rather time consuming. Instead, the simulations are restarted from previously optimised fields, in order to systematically optimise the flows at lower and lower Rm, until Rm_c is identified. To ensure that the global maximum has been achieved, a separate optimisation with a random restart is conducted at Rm_c. The results of these two optimisations are consistent for all three flows. Furthermore, the flows were checked independently using an eigenvalue solver, which confirms the magnetic field growth rate produced and the convergence of the solutions, as shown in Table 2. The optimal magnetic field was always found to be composed of $m = 1$ modes. The dynamos with a toroidal $\ell = 1$ mode are oscillatory, whereas the $t_2^0 s_2^0$ dynamo is steady. The same is true for the original DJ

(n_{max}, ℓ_{max})	$\gamma(t_1^0 s_1^0)$	$\gamma(t_1^0 s_2^0)$	$\gamma(t_2^0 s_2^0)$
$(30, 30)$	$0.00115785514 \pm 0.03052836772i$	$0.00163169179 \pm 1.65823279695i$	$0.00399936144 \pm 0i$
$(40, 40)$	$0.00115785506 \pm 0.03052836773i$	$0.00163171018 \pm 1.65823279861i$	$0.00399936800 \pm 0i$
$(50, 50)$	$0.00115785537 \pm 0.03052836778i$	$0.00163171123 \pm 1.65823279868i$	$0.00399936778 \pm 0i$

Table 2. Growth rates γ for the $m = 1$ $\mathbf{B}_T$ mode, produced by the optimal flows at Rm_c. The growth rates were calculated at resolutions $(n_{max}, l_{max}) = (30, 30), (40, 40)$ and $(50, 50)$ using the eigenvalue solver. The growth rates converge well for all three flows, confirming the veracity of our results. The growth rates obtained from the optimization code for the $t_1^0 s_1^0$, $t_1^0 s_2^0$ and $t_2^0 s_2^0$ at resolution $(40, 40)$ are 0.0011, 0.0012 and 0.005 respectively.
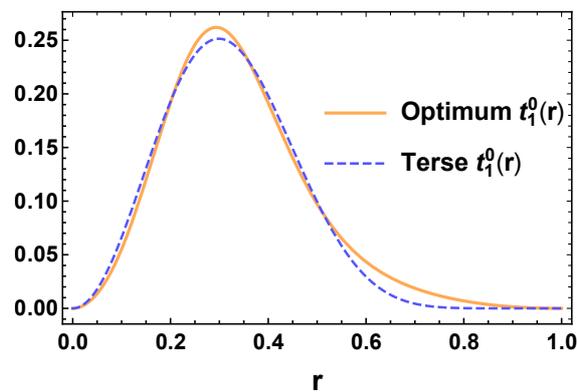
Figure 2. The orange line is the optimal t_1^0 radial basis function plotted as function of r, whereas the blue line is the terse analytical approximation to the toroidal part of the $t_1^0 s_1^0$ flow, satisfying the required symmetry and boundary conditions.

flows. Typically, $\alpha\omega$ dynamos are oscillatory, whereas α^2 dynamos are steady [19]. However, it is not easy to isolate these mechanisms in our solutions, which all appear to have a significant contribution from the shearing velocity (plots of the ϕ components of the flow are provided in the supplemental material).

(b) Terse flows

The optimised flows can be approximated by analytical functions, i.e. simplified into a *terse* form which may be easily reproduced in subsequent studies, without requiring the cumbersome radial basis functions. The terse functions were obtained by fitting the solutions with simple polynomial and sinusoidal functions in r using a non-linear least squares regression, keeping in mind both the symmetry of the flows and the no-slip boundary conditions. Figure 2 shows the fit between the terse and optimum $t_1^0(r)$ radial function. The analytical form of the terse flows is presented in Table 3.

Naturally there is a trade off between simplicity and optimality, however this was found to be quite small. The critical Rm for the terse flows was checked both with a forward run and using the eigenvalue solver. As shown in Tables 1, 3 and 4, Rm_c is $< 12\%$ higher for any of the terse flows, which is not very significant in the range of Rm considered.

(c) Flow structure in physical space

Meridional and equatorial plots of the optimised flows are presented in figures 3 and 4. Figures 5-7 show the spatial structure of the optimised velocity and magnetic field at time T of the three

Flow type	Toroidal rad. function	Poloidal rad. function	Rm_c	γ
$t_1^0 s_1^0$	$0.792(1-r^2)^7 \sin^2(\pi r)$	$0.076(1-r^2)^3 \sin^2(\pi r)$	120.31	$0.00119201224 \pm$ $1.95689566474i$
$t_1^0 s_2^0$	$0.557(1-r^2)^3 \sin^2(\pi r)$	$0.023(1-r^2) \sin^3(\pi r)$	159.66	$0.00036943245\pm$ $1.25906575369i$
$t_2^0 s_2^0$	$0.190(1-r^2) \sin^3(\pi r)$	$0.023(1-r^2) \sin^3(\pi r)$	131.54	$0.00043598313\pm$ $0i$

Table 3. Analytical approximations to the optimised flows' toroidal and poloidal radial functions, i.e. the *terse* flows. The last column gives their growth rate near Rm_c for a resolution of $(n_{max}, l_{max}) = (50, 50)$ measured by the eigenvalue solver code. These approximate values of Rm_c are not significantly higher than those of the optimal flows presented in Table 1.

	$\gamma(t_1^0 s_1^0)$	$\gamma(t_1^0 s_2^0)$	$\gamma(t_2^0 s_2^0)$
Rm	120.31	159.66	131.54
(30,30)	$0.00119201169 \pm 1.95689566479i$	$0.00036943438 \pm 1.25906575473i$	$0.00043597869 \pm 0i$
(40,40)	$0.00119201166 \pm 1.95689566483i$	$0.00036943353 \pm 1.25906575398i$	$0.00043598311 \pm 0i$
(50,50)	$0.00119201224 \pm 1.95689566474i$	$0.00036943245 \pm 1.25906575369i$	$0.00043598313 \pm 0i$

Table 4. Growth rates γ for the $m = 1$ $\mathbf{B}_T$ mode, produced by the terse flows at resolutions $(n_{max}, l_{max}) = (30, 30)$, $(40, 40)$ and $(50, 50)$ with the eigenvalue solver code.

(a)　　　　(b)　　　　(c)
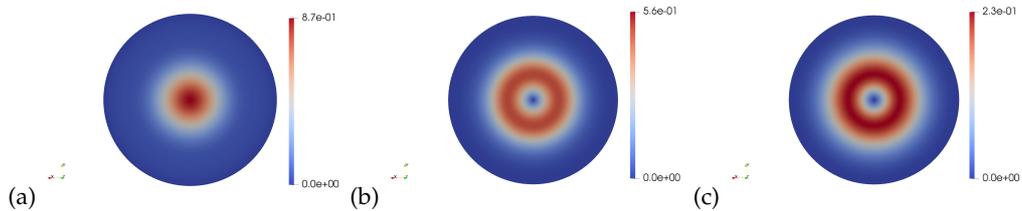
Figure 3. Equatorial sections of the sphere showing the magnitude of $\mathbf{U}$ for the optimal flows (a) $t_1^0 s_1^0$, (b) $t_1^0 s_2^0$ and (c) $t_2^0 s_2^0$.

(a)　　　　(b)　　　　(c)
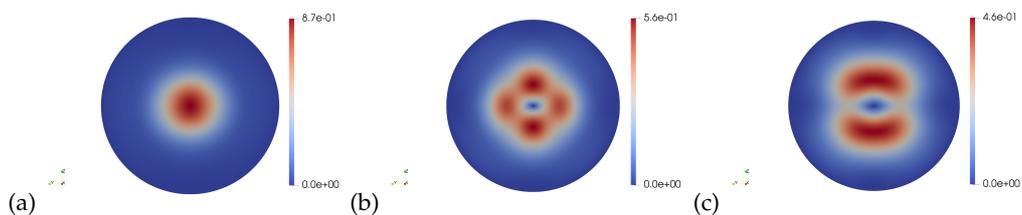
Figure 4. Meridional sections of the sphere showing the magnitude of $\mathbf{U}$ for the optimal flows (a) $t_1^0 s_1^0$, (b) $t_1^0 s_2^0$ and (c) $t_2^0 s_2^0$.
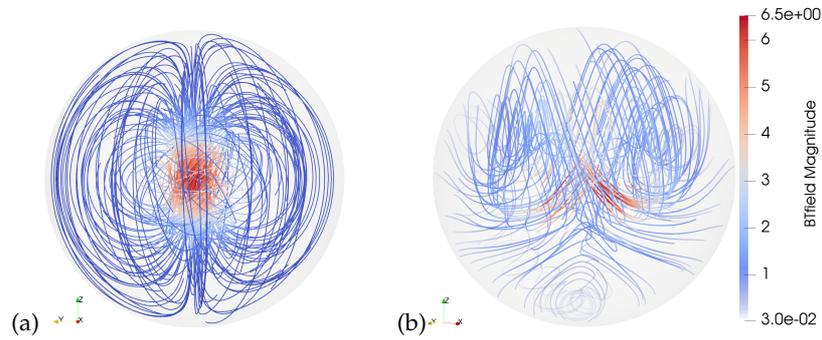
Figure 5. (a) Streamlines of U and (b) magnetic field lines of $\mathbf{B}_T$ for the optimised $t_1^0 s_1^0$ dynamo.
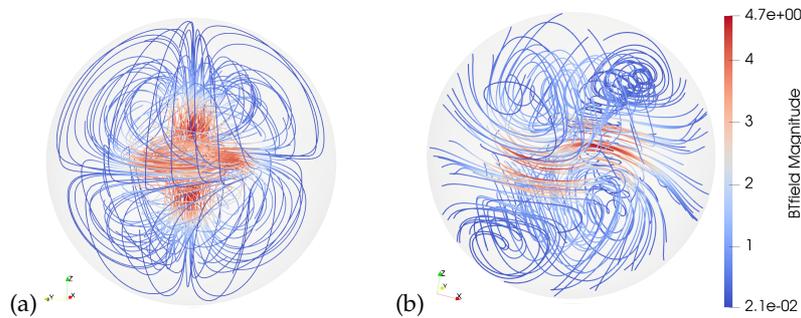
Figure 6. (a) Streamlines of U and (b) magnetic field lines of $\mathbf{B}_T$ for the optimised $t_1^0 s_2^0$ dynamo.

flows within the sphere (i.e. $r \in [0, 1]$). The streamlines are colour coded according to the intensity of the field: red indicates faster flows, blue slower ones. The $t_1^0 s_1^0$ velocity streamlines shown in figure 5(a) display a weak north to south directed meridional flow in the outer half of the sphere, which is regenerated by a strong south to north flow in the centre. The $t_1^0 s_1^0$ $\mathbf{B}_T$ field lines are shown in figure 5(b). Similarly to the velocity, the magnetic field intensity is strongest in the inner 25% of the sphere, where the field twists into oppositely directed branches which join again in the upper hemisphere. Figure 6(a) illustrates the $t_1^0 s_2^0$ velocity streamlines, which run from the poles to the equator. The $t_1^0 s_2^0$ peak velocity is $\sim 65\%$ the intensity of the peak $t_1^0 s_1^0$ flow. In contrast to the latter, there are high intensity regions out to $r \sim 0.45$ and a low velocity patch in the very centre of the sphere. This radial intensity variation can also be seen in the $\mathbf{B}_T$ field, whose structure is shown in figure 6(b). The field is strongest at intermediate radii, becoming less intense near the centre. The $t_2^0 s_2^0$ velocity field has a peak intensity of only 53% that of the $t_1^0 s_1^0$ flow. As shown in figure 7(a), the flow along the axis travels rapidly towards the poles, with a slow back-flow in the outer region and very low velocities in the equatorial plane. Figure 7(b) shows that the magnetic field is most intense in the centre, where it twists. The highest flow magnitudes are within $r < 0.25$, with low speeds in the outer regions.

The velocity and vorticity fields are well aligned in the inner half of the sphere for both the $t_1^0 s_1^0$ and $t_2^0 s_2^0$ flows, such that these flows have large pointwise helicities, as shown in figures 8(a) and 8(b). The alignment between velocity and vorticity persists up to larger radii compared to Chen et al. [10]'s solution. It is not present in any region of the sphere for the $t_1^0 s_2^0$ case (figure 8(b)), resulting in lower overall helicity.

The alignment corroborates the work of many authors ([18], [21], [22]) who found that flows which display greater helicity allow for more efficient dynamo action. At the onset of dynamo action, the external magnetic field $\mathbf{B}_T$ for all flows is dipolar, as shown in figure 9. This is because
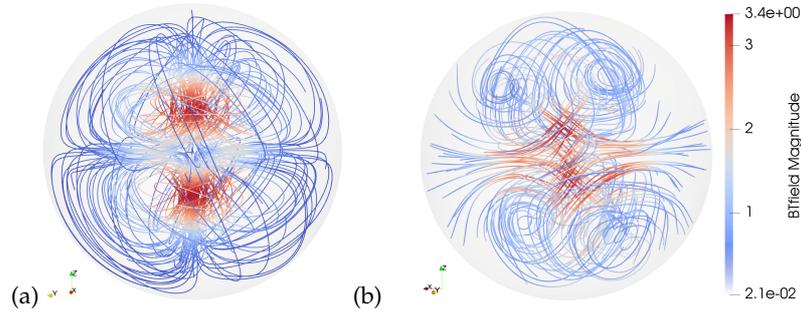
Figure 7. a) Streamlines of U and (b) magnetic field lines of $\mathbf{B}_T$ for the optimised $t_2^0 s_2^0$ dynamo.
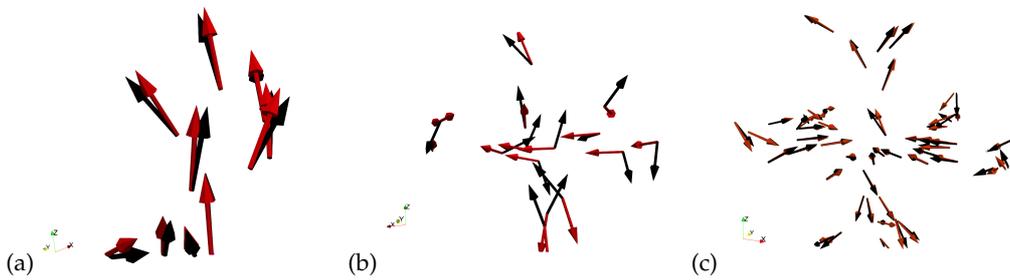
Figure 8. (a) $t_1^0 s_1^0$ for $r \leq 0.325$ (b) $t_1^0 s_2^0$ for $r \leq 0.5$ (c) $t_2^0 s_2^0$ for $r \leq 0.75$. The arrows show the direction of the velocity (red) and vorticity (black) fields for the $t_1^0 s_1^0$ (left), $t_1^0 s_2^0$ (centre) and $t_2^0 s_2^0$ (right) flows. The $t_1^0 s_2^0$ flow doesn't display any significant local alignment. A subspace of the unit sphere is shown to highlight the alignment of the velocity and vorticity.
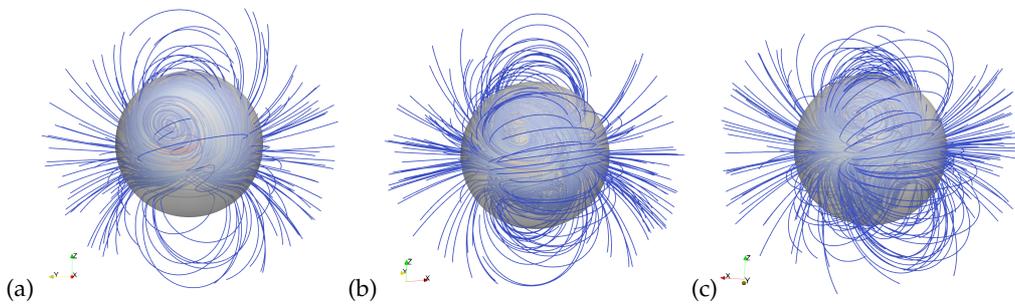
Figure 9. External magnetic fields for the (a) $t_1^0 s_1^0$ (b) $t_1^0 s_2^0$ and (c) $t_2^0 s_2^0$ flows up to $r = 2$, shown in the same orientation as in figures 5(b), 6(b) and 7(b). All fields are dipolar.

the $m = 1$ magnetic modes have the largest real growth rate, as mentioned in section 3(a). Both the $t_1^0 s_1^0$ and $t_2^0 s_2^0$ flows produce magnetic fields which do not display a specific symmetry; $\mathbf{B}_T$ contains all ℓ modes, with both cosine and sine harmonic contributions. The $t_1^0 s_2^0$ flow, on the other hand, is symmetric with respect to a reflection in the equatorial plane, and antisymmetric with respect to a rotation through π radians about the $\theta = 0$ axis. Thus, it only contains the modes:

$$S_1^{1c}, S_1^{1s}, T_2^{1c}, T_2^{1s}, S_3^{1c}, S_3^{1s}, \dots$$

Investigating the angularly averaged properties of these optimised flows can also be useful, as they might highlight radial structures which are important for dynamo action. The radial distribution of a given quantity is found by taking the average over solid angle.
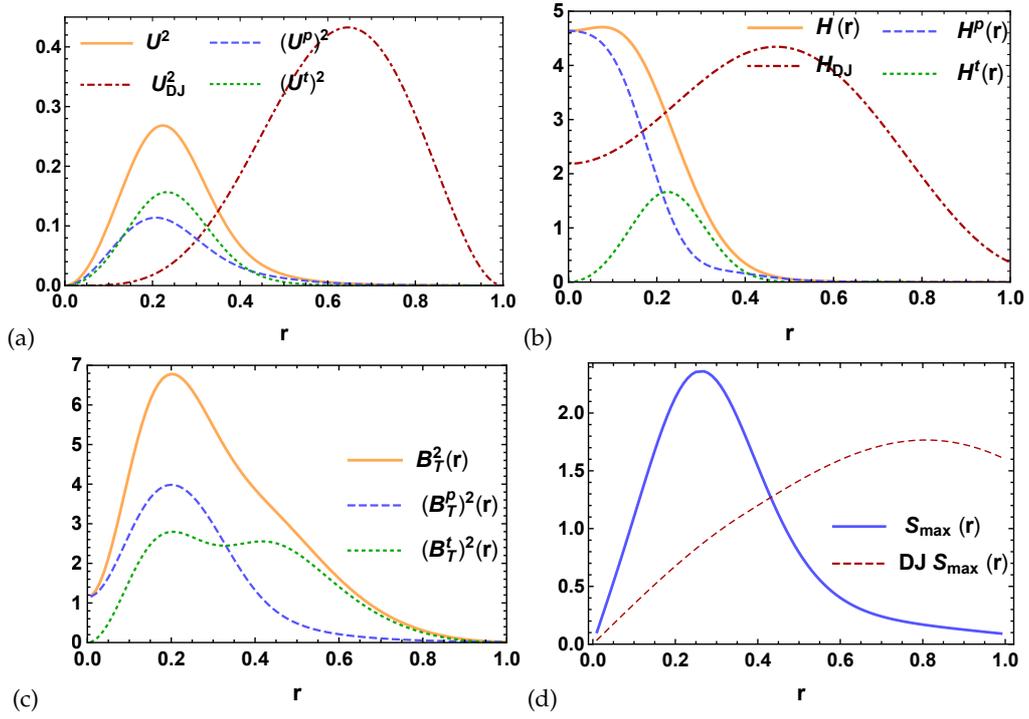
Figure 10. Radial distributions of (a) kinetic energy, (b) helicity, (c) magnetic energy and (d) maximum strain rate for the $t_1^0 s_1^0$ optimised solution, including profiles of the original DJ flow for reference.
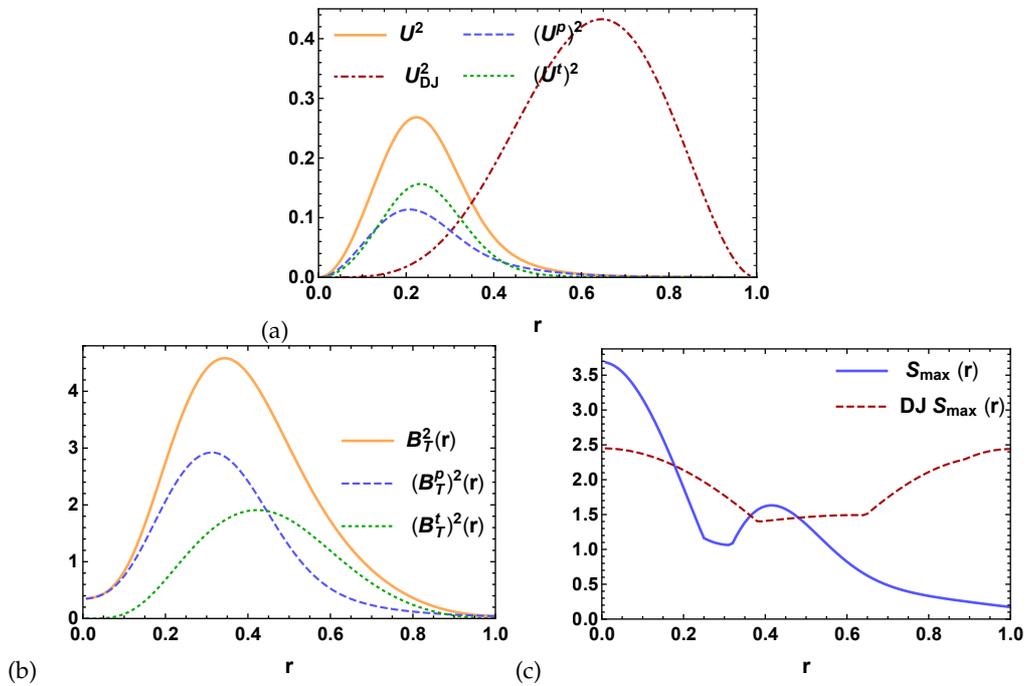
Figure 11. Radial distributions of (a) kinetic energy, (b) helicity, (c) magnetic energy and (d) maximum strain rate for the $t_1^0 s_2^0$ optimised solution, including profiles of the original DJ flow for reference. Helicity averaged over solid angle is identically zero for this flow, due to the presence of different spherical harmonic components.
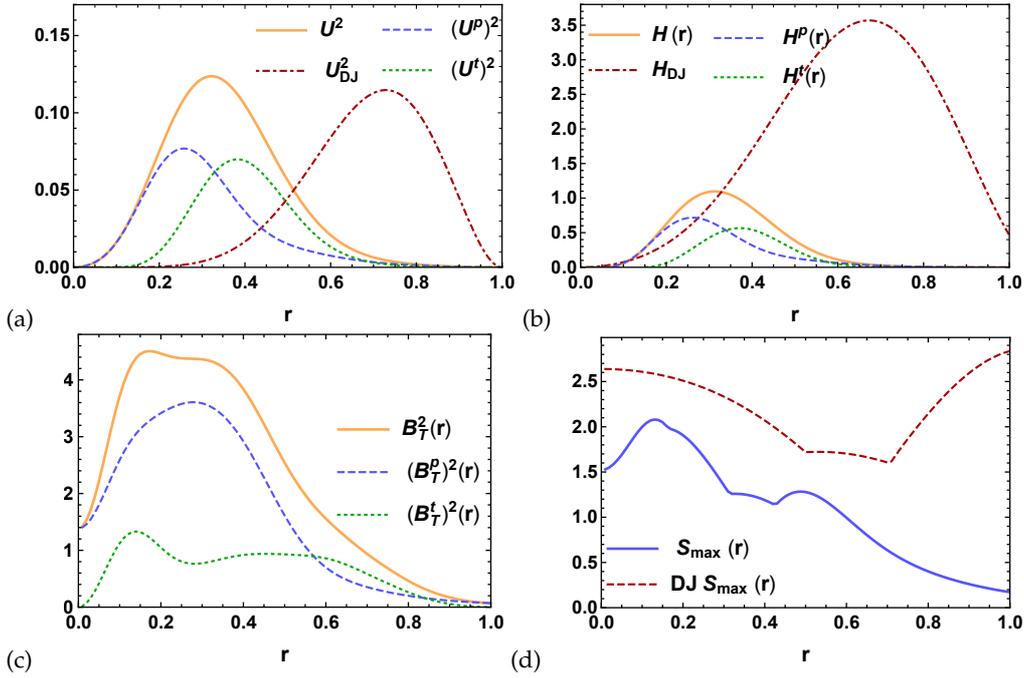
Figure 12. Radial distributions of (a) kinetic energy, (b) helicity, (c) magnetic energy and (d) maximum strain rate for the $t_2^0 s_2^0$ optimised solution, including profiles of the original DJ flow for reference.

For example, the radial magnetic energy distribution is:

$$B_T(r)^2 = \frac{1}{4\pi} \int_0^{2\pi} \int_0^{\pi} (\mathbf{B}_T^t)^2 + (\mathbf{B}_T^p)^2 \sin\theta \, \mathrm{d}\theta \, \mathrm{d}\phi \qquad (3.1)$$

An analogous expression produces the radial kinetic energy and helicity distributions, keeping in mind that the helicity components are:

$$H^p(r) = \frac{1}{4\pi} \int_0^{2\pi} \int_0^{\pi} \mathbf{U}^p \cdot \nabla \times \mathbf{U}^t \sin\theta \, \mathrm{d}\theta \, \mathrm{d}\phi \quad H^t(r) = \frac{1}{4\pi} \int_0^{2\pi} \int_0^{\pi} \mathbf{U}^t \cdot \nabla \times \mathbf{U}^p \sin\theta \, \mathrm{d}\theta \, \mathrm{d}\phi \quad (3.2)$$

In addition, we consider the radial distribution of shear. Shear is important for processes such as the Omega effect, where it helps to transform poloidal magnetic field into toroidal field [23]. Regions with most shear are thus likely to be associated with magnetic field generation. The radial profile of the maximum shear at a given point, S_{max}, can be quantified via the maximum absolute strain rate, through:

$$S_{max}(r) = \max_{r \in V} |\mathrm{eig}(\nabla \mathbf{U} + \nabla \mathbf{U}^T)/2| \qquad (3.3)$$

The angularly averaged properties of the $t_1^0 s_1^0$ flow in figure 10 present distinct similarities to the optimal flow found by Chen et al. [10], despite the physical flow structure being quite different. The helicity and kinetic energy profiles are quite similar, peaking near the centre of the sphere (at $r = 0$ and $r = 0.08$ respectively) and again demonstrating the velocity-vorticity alignment. This can also be observed in the $t_2^0 s_2^0$ profile (figure 12), although here the peaks are both shifted towards $r = 0.3$, due to the greater number of circulation cells. The kinetic energy of the $t_1^0 s_2^0$ flow, shown in figure 11, peaks at $r = 0.22$, an intermediate radius compared to the single ℓ flows.

The flow is nearly stagnant in the outer half of the sphere for $t_1^0 s_1^0$, which was also observed by Chen et al. [10]. In fact, all flows have a sluggish layer spanning at the least the outer 20% of the sphere. Bullard and Gubbins [24] suggested that such a layer could improve dynamo action by reducing energy loss by magnetic diffusion.

In the $t_1^0 s_1^0$ case, the total magnetic energy appears to follow the shear, with both quantities reaching a maximum near $r = 0.2$, albeit not exactly at the same position. The $t_2^0 s_2^0$ $\mathbf{B}_T$ field also appears to peak in a similar location to the maximum shear, however shear variations at larger r are not mirrored closely. In the $t_1^0 s_2^0$ case, the magnetic field generation does not appear to be linked to the shear. Therefore, although in many cases shearing can amplify the magnetic field through an Omega-type effect, this mechanism is not necessarily present in all optimised dynamos, but appears to act in the more efficient ones.

(d) Spectral analysis of flow fields

The solutions' convergence can also be verified by looking at the spectra of the optimised flows. Figures 13(a)-(c) shows the magnetic energy and squared enstrophy in each n mode, while figures 13(d)-(f) give the magnetic energy in each ℓ mode. These were computed using the partial sums:

$$\mathbf{B}_n = \sum_{m,\ell} T_{nm\ell}\mathbf{B}^t_{nm\ell} + S_{nm\ell}\mathbf{B}^p_{nm\ell} \tag{3.4}$$

An analogous expression can be written for $\mathbf{U}_n$ and the ℓ spectrum. The enstrophy spectra include at most two distinct ℓ modes and as such are not very smooth. Nonetheless, they do follow a linear trend, which indicates the exponential convergence typical of spectral methods [25]. The magnetic field spectra are much smoother, due to the averaging effect of including all ℓ modes. Chen et al. [10] provide spectra with respect to ℓ. When their results are plotted against n, comparable convergence rates are found for their velocity field, while the magnetic field solutions found here converge more rapidly.

(e) Comparison to theoretical bounds and optimal dynamo for a sphere

The magnetic Reynolds numbers for each flow can be compared to theoretically determined lower bounds for dynamo action, to see how far above this minimum requirement the dynamos are operating. In particular, we consider the Backus and Childress bounds, based on maximum strain and velocity respectively:

$$\text{Backus} : Rm^s > \pi^2$$

$$\text{Childress} : Rm\, U_{max} > \pi$$

The definitions for different Rm conventions are given in section 2(a). A comparison was also made with the bound of Proctor [26], however this was not particularly applicable as the bound is most useful in the limit $\mathbf{U}^p \to 0$, which does not hold in our case. Table 5 presents the energy, enstrophy and strain based Rm_c for each optimised flow, as well as their proximity to the theoretical bounds defined above. For comparison, these same quantities are reported for the original DJ flows and the optimum dynamo in a sphere. The optimised flows operate at significantly reduced Rm_c compared to the original DJ flows (save for the strain-based Rm^s), but still 18-30 times above the Childress bound and 30-50 times above the Backus bound. The $t_1^0 s_1^0$ flow shows the greatest improvement, with an enstrophy-based Rm_c which is more than four times smaller than the original onset for dynamo action. The $t_1^0 s_2^0$ flow's Rm_c has been reduced by more than a factor of 2, while the $t_2^0 s_2^0$ flow's Rm_c is now 35% smaller. The root-mean squared speeds of the optimised flows are at least four times smaller than the original DJ flows', while their maximum strain rates remain comparable. The optimised axisymmetric flows' Rm_c are similar to that of the overall optimum flow for a sphere, differing at most by a factor of 2.2.
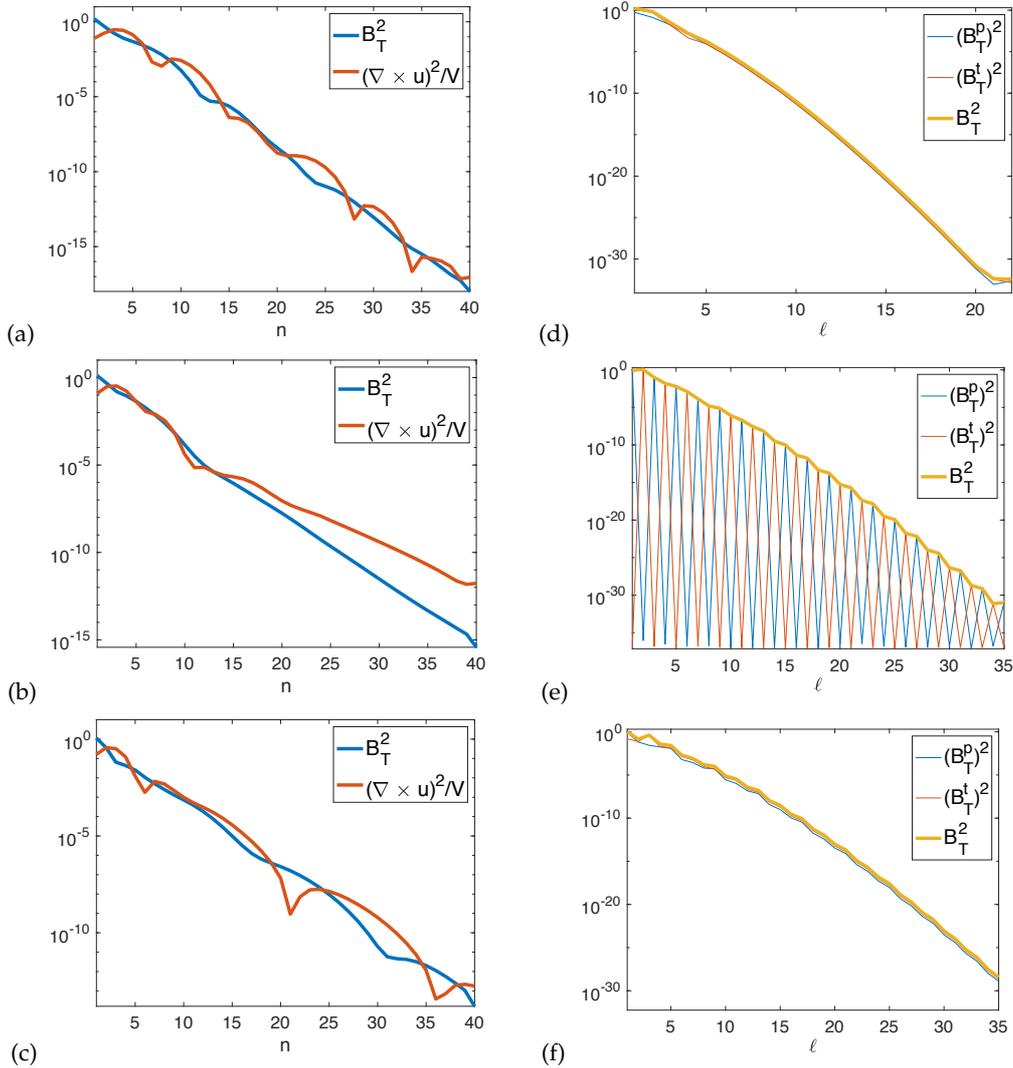
Figure 13. Final magnetic energy (blue) and kinetic energy (red) for: each n mode of the optimised flows (a) $t_1^0 s_1^0$, (b) $t_1^0 s_2^0$, (c) $t_2^0 s_2^0$ and each l mode (d) $t_1^0 s_1^0$, (e) $t_1^0 s_2^0$, (f) $t_2^0 s_2^0$. Panel (e) shows the symmetry separation of the $t_1^0 s_2^0$ $\mathbf{B}_T$ solution, where the poloidal and toroidal component only contain odd and even ℓ modes respectively.

The most efficient axisymmetric flow is the $t_1^0 s_1^0$, which displays very similar characteristics to the optimum of Chen et al. [10]. This was expected, as their flow is dominated by t_1^0 and s_1^0 modes. The physical structure of the resulting magnetic field is comparable, with two main branches and a central twist (compare to figure 4 of [10]). The angularly averaged properties are also very similar in form and magnitude. The main difference is an extended contribution to the toroidal magnetic field beyond $r \sim 0.3$ for the axisymmetric flow. The overall optimal axisymmetric flow without restriction on the number of modes present was also computed, and was found to have $Rm_c = 96.38$. This result agrees with a previous study [27], and is only 10% smaller than the Rm_c of the $t_1^0 s_1^0$ flow. Streamlines of the optimal $\mathbf{U}$ and $\mathbf{B}_T$ are presented in Figure 14. The optimal flow is dominated by the first three ℓ modes, with the $\ell = 2$ providing the largest contribution. Overall the $\ell = 1 - 3$ modes account for over 90% of the enstrophy. The region of maximal velocity is offset from the sphere's centre, in contrast to the DJ optima. The optimal magnetic field is again dipolar, containing all ℓ modes, and so does not display specific symmetries.
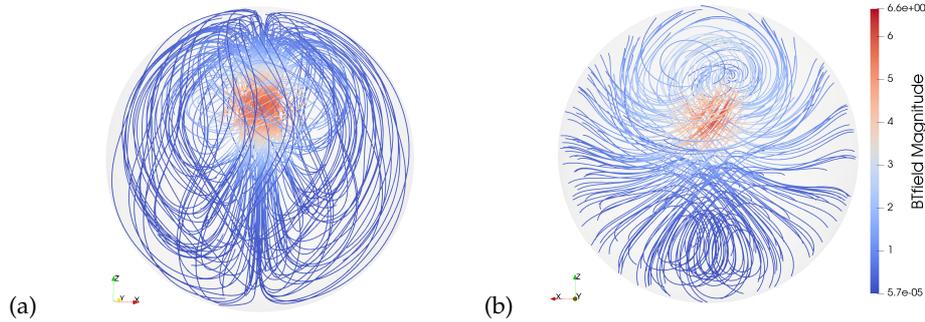
Figure 14. a) Streamlines of U and (b) magnetic field lines of $\mathbf{B}_T$ for the optimised axisymmetric dynamo, in which all $m = 0$ flow modes are allowed.

	Rm_c^u	Rm_c	S_{max}	Rm_c^s	Rm_c^s/π^2	U_{rms}	U_{max}	$Rm_c U_{max}/\pi$
$t_1^0 s_1^0$	13.7	107.70	2.36	254.7	25.8	0.13	0.87	29.8
$t_1^0 s_2^0$	19.6	142.42	3.68	524.5	53.1	0.14	0.56	25.5
$t_2^0 s_2^0$	16.4	125.50	2.08	261.1	26.5	0.13	0.46	18.2
Axisymmetric	13.0	96.38	2.02	194.7	19.7	0.14	0.77	23.6
DJ $t_1^0 s_1^0$	104	476	1.77	274	27.8	0.67	1.12	169.7
DJ $t_1^0 s_2^0$	60	310	2.45	233	23.6	0.64	1.07	105.6
DJ $t_2^0 s_2^0$	32	193	2.84	153	15.5	0.59	0.94	57.7
Unconstrained	7.0	64.45	3.33	215	21.8	0.11	0.69	14.2

Table 5. Quantitative comparison between the new optima, the overall optimum for axisymmetric flows, the classical Dudley-James flows and Chen et al. [10]'s optimum for flows in a sphere. The second, third and fifth columns give the energy, enstrophy and strain based Rm_c respectively. S_{max} and U_{max} are the maximum strain and velocity magnitudes present in the flow. U_{rms} is the root-mean square velocity of the flow. The sixth and ninth columns provide a comparison with the Backus and Childress bounds respectively.

Chen et al. [10] found that the maximum strain rate appears to be correlated with the radially averaged B_T field. We see this correlation for the $t_1^0 s_1^0$ flow, and to a certain extent for the $t_2^0 s_2^0$ flow, however the mixed ℓ field does not display any obvious connection between these two properties. This may be another reason why the $t_1^0 s_2^0$ flow is less efficient.

It is important to note that the choice of Rm convention strongly influences the form of the resulting flows. The enstrophy-based Rm does not place a restriction on the system's local maximum strain, so the optima do not necessarily have a lower Rm^s than the original flows. However, due to the use of no-slip boundary conditions, the root mean enstrophy is equal to the global shear magnitude [10], which is small. Thus, our optimisation selects flows with moderate velocities which do not present strong gradients perpendicular to the flow and might therefore be more likely to occur in a physical setting for sustained periods of time.

4. Conclusions

In this paper, we optimised three axisymmetric flows to find the lowest magnetic Reynolds number for which they operate as kinematic dynamos. The form of these flows was originally

proposed by Dudley and James [9]. A modified variant of the Lagrangian optimization procedure developed by Chen et al. [10] was applied in conjunction with a Galerkin basis to optimise the spectral coefficients of the fluid flow and initial magnetic field. This work extends Chen et al. [10]'s optimisation method, which finds the most efficient unconstrained flows in a sphere, to flows containing only two modes. The optimal flows were found to have enstrophy-based values of Rm_c of $107.7, 142.4$ and 125.5 for the $t_1^0 s_1^0$, $t_1^0 s_2^0$ and $t_2^0 s_2^0$ modes respectively, up to four times smaller than the original DJ bounds. The flows containing the same toroidal and poloidal ℓ have strain-based values of Rm_c which are ~ 26 times the Backus bound, while the Rm_c for the flow containing mixed ℓ modes is 53 times the Backus bound. The magnetic field growth rates and the convergence of the solutions were corroborated using a numerical eigenvalue solver. The optimised flows' radial functions were fitted with analytical expressions obeying the same boundary conditions and symmetry constraints, producing *terse* flows, whose Rm_c is at most 12% higher. Compared to the original flows, all three optimised dynamos have quite similar values of Rm_c, with the single ℓ-mode flows being slightly more efficient. These flows display an alignment of velocity and vorticity in the inner third of the sphere, resulting in large point-wise helicity. On the other hand, the $t_1^0 s_2^0$ flow does not display such an alignment, further confirming the observations of previous authors ([18], [28]) that helicity improves a dynamo's efficiency. Our results also corroborate previous observations ([24], [10]) that the presence of a nearly stagnant layer near the surface of the sphere promotes dynamo action, as all three optimised flows have very low velocities near the edge of the fluid container.

Overall, these are some of the simplest and most efficient kinematic dynamos known to exist. We hope that the simple form of the terse flows might make them a useful reference for future studies, and perhaps form the basis for an experimental dynamo.

A. Magnetic Reynolds number conversion formulae

The enstrophy-based magnetic Reynolds number, Rm, defined in section 2(a) can be converted to the more conventional energy (Rm^u) and strain based (Rm^s) definitions through the following relations:

$$Rm^u = \left(\sqrt{\frac{1}{V} \int_V \mathbf{U}^2 \, \mathrm{d}V} \right) Rm \qquad \text{where} \qquad Rm^u = \frac{U^* L^*}{\eta^*}$$

$$Rm^s = \left(\max_V |\mathrm{eig}(\nabla \mathbf{U} + \nabla \mathbf{U}^T)/2| \right) Rm = S_{max} Rm \qquad \text{where} \qquad Rm^s = \frac{S_{max}^* L^{*2}}{\eta^*}$$

The notation is the same as in the main body of the paper, with the asterisk denoting dimensional quantities. We note that our optimisation focuses on the enstrophy of the flow, not the strain, so that the Rm^s of the optimised flows may be higher than that reported by similar flows in other studies, e.g. [29].

B. Galerkin basis radial functions

The magnetic field, $\mathbf{B}$, radial functions are:

$$\mathcal{T}_n^\ell(r) = N_{n,\ell}^h r^{\ell+1}(1-r^2)P_{n-1}^{(2,\ell+1/2)}(2r^2-1)$$

$$\mathcal{P}_n^\ell(r) = N_{n,\ell}^k r^{\ell+1}(c_1 P_n^{(0,\ell+1/2)}(2r^2-1) + c_2 P_{n-1}^{(0,\ell+1/2)}(2r^2-1))$$

(A 1)

With

$$c_1 = n(2\ell + 2n - 1), \qquad c_2 = -(n+1)(2n+2\ell+1)$$

(A 2)

The velocity field, $\mathbf{U}$, radial functions are:

$$t_n^\ell(r) = N_{n,\ell}^f r^{\ell+1}(P_n^{(0,\ell+1/2)}(2r^2-1) - P_{n-1}^{(0,\ell+1/2)}(2r^2-1))$$

$$p_n^\ell(r) = N_{n,\ell}^g r^{\ell+1}\sum_{i=1}^3 c_i P_{n+2-i}^{(0,\ell+1/2)}(2r^2-1)$$

(A 3)

With

$$c_1 = 2\ell + 4n + 1, \qquad c_2 = -2(2\ell + 4n + 3), \qquad c_3 = 2\ell + 4n + 5$$

(A 4)

$P_n^{(\alpha,\beta)}$ are Jacobi Polynomials and $N_{\alpha,\beta}^\gamma$ are normalisation factors ensuring the basis' orthonormality. The boundary conditions satisfied by the basis fields are:

$$t_n^\ell(1) = 0, \qquad p_n^\ell(1) = \frac{\partial p_n^\ell}{\partial r}(1) = 0, \qquad \mathcal{T}_n^\ell(1) = 0, \qquad \frac{\partial \mathcal{P}_n^\ell(1)}{\partial r} + \ell\mathcal{P}_n^\ell(1) = 0$$

(A 5)

C. Form of DJ flows

The explicit forms of the three DJ flows are given below.

$$t_1^0 s_1^0 : \qquad \mathbf{U}(r,\theta,\phi) = \nabla \times (t_1^0(r)Y_1^0(\theta,\phi)\hat{\mathbf{r}}) + \nabla \times \nabla \times (p_1^0(r)Y_1^0(\theta,\phi)\hat{\mathbf{r}})$$

(A 1)

$$t_1^0 s_2^0 : \qquad \mathbf{U}(r,\theta,\phi) = \nabla \times (t_1^0(r)Y_1^0(\theta,\phi)\hat{\mathbf{r}}) + \nabla \times \nabla \times (p_2^0(r)Y_2^0(\theta,\phi)\hat{\mathbf{r}})$$

(A 2)

$$t_2^0 s_2^0 : \qquad \mathbf{U}(r,\theta,\phi) = \nabla \times (t_2^0(r)Y_2^0(\theta,\phi)\hat{\mathbf{r}}) + \nabla \times \nabla \times (p_2^0(r)Y_2^0(\theta,\phi)\hat{\mathbf{r}})$$

(A 3)

(A 4)

We use fully normalised spherical harmonics, which satisfy:

$$\int_{\theta=0}^\pi \int_{\phi=0}^{2\pi} Y_\ell^m Y_{\ell'}^{m'} d\Omega = \delta_{\ell\ell'}\delta_{mm'}$$

(A 5)

The radial functions used by Dudley and James [9] are:

$$t_1^0(r) = \sqrt{\frac{4\pi}{3}} r\sin(\pi r), \qquad\qquad t_2^0(r) = \sqrt{\frac{4\pi}{5}} r^2\sin(\pi r)$$

(A 6)

$$s_1^0(r) = \varepsilon\sqrt{\frac{4\pi}{3}} r\sin(\pi r), \qquad\qquad s_2^0(r) = \varepsilon\sqrt{\frac{4\pi}{5}} r^2\sin(\pi r)$$

(A 7)

(A 8)

where $\varepsilon = 0.17, 0.13$ and 0.14 for the $t_1^0 s_1^0$, $t_1^0 s_2^0$ and $t_2^0 s_2^0$ flows respectively. The numerical prefactors appear because Dudley and James [9] use a *Neumann normalisation* for spherical harmonics:

$$\int_{\theta=0}^{\pi} \int_{\phi=0}^{2\pi} Y_\ell^m Y_{\ell'}^{m'} d\Omega = \frac{4\pi}{2\ell+1} \left[\frac{(\ell+m)!}{(2-\delta_{m0})(\ell-m)!} \right] \delta_{\ell\ell'} \delta_{mm'} \tag{A 9}$$

References

1. Roberts, P. H. and King, E.M. 2013 On the genesis of the Earth's magnetism. *Reports on Progress in Physics*, **76**, 096801. (doi:10.1088/0034-4885/76/9/096801)
2. Larmor, J. 1919 How could a rotating body such as the Sun become a magnet? *Rep. Brit. Assoc.* **87**, 159-160.
3. Olson, P. 2007 State of the Core. In *Treatise on Geophysics* (ed. G. Schubert), vol. **8**, pp. 3-6. Amsterdam, The Netherlands: Elsevier.
4. Bullard, E. C. and Gellman, H. 1954 Homogeneous dynamos and terrestrial magnetism. *Proc. R. Soc. A* **247**, 213-278.
5. Roberts, G.O. 1971 Reported by P.H. Roberts in *World magnetic surveys 1957-1969* (ed. A. J. Zmuda), pp. 123-131. Paris: International Union of Geodesy and Geophysics Publication Office.
6. Gubbins, D. 1973 Numerical solutions of the kinematic dynamo problem. *Proc. R. Soc. A* **274**, 493-521.
7. Pekeris, C.L., Accad, Y. and Shkoller, B. 1973 Kinematic dynamos and the Earth's magnetic field. *Phil. Trans. R. Soc. A* **275**, 425-461.
8. Kumar, S. and Roberts, P. H. 1975 A three-dimensional kinematic dynamo. *Proc. R. Soc. Lond. A* **344**, 235-258.
9. Dudley, M. L. and James, R. W. 1989 Time-dependent kinematic dynamos with stationary flows. *Proc. R. Soc. A* **425**, 407-429. (doi:10.1098/rspa.1989.0112)
10. Chen, L. and Herreman, W. and Li, K. and Livermore, P.W. and Luo, J.W. and Jackson, A. 2018 The optimal kinematic dynamo driven by steady flows in a sphere. *J. Fluid Mech.* **839**, 1-32. (doi:10.1017/jfm.2017.924)
11. Pringle, C. C. T. and Kerswell, R. R. 2010 Using Nonlinear Transient Growth to Construct the Minimal Seed for Shear Flow Turbulence. *Phys. Rev. Lett.* **105**, 154502. (doi:0.1103/PhysRevLett.105.154502)
12. Pringle, C. C. T., Willis A.P. and Kerswell, R. R. 2012 Minimal seeds for shear flow turbulence: using nonlinear transient growth to touch the edge of chaos. *J. Fluid Mech.* **702**, 415-443. (doi:10.1017/jfm.2012.192)
13. Kerswell, R.R. 2018 Nonlinear Nonmodal Stability Theory. *Ann. Rev. Fluid Mech.* **50**, 319-345. (doi:10.1146/annurev-fluid-122316-045042)
14. Willis, A. P. 2012 Optimization of the Magnetic Dynamo. *Phys. Rev. Lett.*, **109** (25), 251101. (doi:10.1103/PhysRevLett.109.251101)
15. Chen, L., Herreman, W. and Jackson, A. 2015 Optimal dynamo action by steady flows confined in a cube. *J. Fluid Mech.* **783**, 23-45. (doi:10.1017/jfm.2015.545)
16. Monchaux, R., Berhanu, M., Aumaître, S., Chiffaudel, A., Daviaud, F., Dubrulle, B., Ravelet, F., Fauve, S., Mordant, N., Pétrélis, F., Bourgoin, M., Odier, P., Pinton, J., Plihon, N. and Volk, R. 2009 The von Kármán Sodium experiment: Turbulent dynamical dynamos. *Physics of Fluids*, **21** (3), 035108. (doi:10.1063/1.3085724)
17. Proctor, M. R. E. 2015 Energy requirement for a working dynamo. *Geophysical & Astrophysical Fluid Dynamics*, **109** (6), 611-614. (doi:10.1080/03091929.2015.1094065)
18. Moffatt, H. K. 1978 *Field generation in electrically conducting fluids.* Cambridge, London, New York, Melbourne: Cambridge University Press.
19. Roberts, P. H, 2007 Theory of the Geodynamo. In *Treatise on Geophysics* (ed. G. Schubert), vol. **8**, pp. 67-105. Amsterdam, The Netherlands: Elsevier.
20. Luchini, P. and Bottaro, A. 2014 Supplemental appendix to Adjoint Equations in Stability Analysis. *Annu. Rev. Fluid Mech.*, **46**, 493-517. (doi:10.1146/annurev-fluid-010313-141253)
21. Nakajima, T. and Kono, M. 1993 Effect of Helicity on the Efficiency of Laminar Kinematic Dynamos. *Journal of geomagnetism and geoelectricity*, **45** (11-12), 1575-1589. (doi:10.5636/jgg.45.1575)
22. Gubbins, D. 2008 Implication of kinematic dynamo studies for the geodynamo. *Geophys. J. Int.*, **173** (1), 79-91. (10.1111/j.1365-246X.2007.03707.x)
23. Jones, C. A. 2008 Course 2: dynamo theory. In Cardin, P. and Cugliandolo, L., editors, *Dynamos*, volume 88 of *Les Houches*, pages 45-135. Elsevier.

24. Bullard, E. C. and Gubbins, D. 1977 Generation of magnetic fields by fluid motions of global scale. *Geophys. Astrophys. Fluid Dyn.* **8** (1), 43-56.

25. Boyd JP. 2001 *Chebyshev and Fourier spectral methods*. New York, NY: Dover.

26. Proctor M.R.E. 2004 An extension of the Toroidal Theorem *Geophys. Astrophys. Fluid Dyn.* **98** (3), 235-240. (doi:10.1080/030919209410001659272)

27. Chen, L. 2018 Optimization of Kinematic Dynamos Using Variational Methods (Doctoral dissertation, ETH Zürich, Switzerland) (doi:10.3929/ethz-b-000227237)

28. Roberts, P. H. and Bullard, E. 1972 Kinematic dynamo models. *Phil. Trans. Roy. Soc. Lon. A, Mathematical and Physical Sciences* **272** (doi:10.1098/rsta.1972.0074)

29. Holme, R. 2003 Optimised axially-symmetric kinematic dynamos. *Physics of the Earth and Planetary Interiors*, **140**, 1, 3-11. (doi:10.1016/j.pepi.2003.07.003)